Physics of Fluids

RESEARCH ARTICLE | SEPTEMBER 13 2023

Energy mechanism for the instability of liquid jets with thermocapillarity

Yu-Wen Sun (孙宇文) ; Kai-Xin Hu (胡开鑫) ; Qi-Sheng Chen (陈启生)

Physics of Fluids 35, 094114 (2023)
https://doi.org/10.1063/5.0166867

Physics of Fluids ARTICLE pubs.aip.org/aip/pof

Energy mechanism for the instability of liquid jets with thermocapillarity

Cite as: Phys. Fluids **35**, 094114 (2023); doi: 10.1063/5.0166867
Submitted: 8 July 2023 · Accepted: 23 August 2023 ·
Published Online: 13 September 2023

View Online Export Citation CrossMark

Yu-Wen Sun (孙宇文),[1,2] Kai-Xin Hu (胡开鑫),[1,2,3,a)] and Qi-Sheng Chen (陈启生)[4,5]

AFFILIATIONS

[1]Zhejiang Provincial Engineering Research Center for the Safety of Pressure Vessel and Pipeline, Ningbo University, Ningbo, Zhejiang 315211, China
[2]Key Laboratory of Impact and Safety Engineering (Ningbo University), Ministry of Education, Ningbo, Zhejiang 315211, China
[3]State Key Laboratory for Turbulence and Complex Systems, College of Engineering, Peking University, Beijing 100871, China
[4]School of Engineering Science, University of Chinese Academy of Sciences, Beijing 100190, China
[5]Key Laboratory of Microgravity, Institute of Mechanics, Chinese Academy of Sciences, Beijing 100190, China

[a)]Author to whom correspondence should be addressed: hukaixin@nbu.edu.cn

ABSTRACT

Xu and Davis [J. Fluid Mech. **161**, 1–25 (1985)] examined the stability of long axisymmetric liquid jet subjected to an axial temperature gradient, finding capillary, surface-wave, and hydrodynamic modes. They showed that capillary breakup can be retarded or even suppressed for a small Prandtl number ($Pr < 1$) and a large Biot number ($Bi \geq 1$). In the present work, the energy mechanism is carried out for these three kinds of flow instabilities, and the mechanism of suppressing capillary breakup is clarified. When the Reynolds number (R_B) is not large, the work done by the pressure on the free surface (P_S) is the main energy source of the capillary instability. At small Pr and large Bi, the phase difference between the radial velocity and surface deformation increases with R_B, leading to the decrease in P_S, which prevents the occurrence of capillary breakup. Meanwhile, the work done by thermocapillary force becomes the main energy source, making hydrodynamic modes unstable. The perturbation flow fields are displayed, which shows that the temperature fluctuations of three modes differ from each other.

I. INTRODUCTION

If a temperature difference exists along a gas–liquid interface, the variation of surface tension will induce a convection in the liquid. This phenomenon is called the thermocapillary effect. Since the pioneering work of Pearson,[1] there has been a much greater understanding in this field. If a liquid jet is exposed to a temperature difference from its surroundings, additional instabilities may arise, which can impact the breakup properties of the jet. This situation is found in various processes, such as inkjet printing,[2,3] fiber preparation,[4] droplet formation,[5,6] injection of rocket engine, and gas turbine.[7,8]

Different types of instabilities may occur based on the direction of temperature gradient. Marangoni instabilities arise from the radial temperature gradient, and extensive research works have been conducted in this area. Imaishi *et al.*[9] have linearly analyzed the effect of the Prandtl number (Pr) on the stability of thermocapillary flow in shallow annular pools. By means of energy budget analysis, they have revealed that instabilities in low-Pr range are hydrodynamic in nature. Conversely, instabilities in the middle- and high-Pr regions are hydrodynamic instabilities. Qiao *et al.*[10] have investigated temporal linear instability of coaxial jets under a radial temperature gradient, exploring the relative importance of various energy components in the most unstable mode through the application of perturbation kinetic energy balance. Li *et al.*[11] have analyzed the stability of thermocapillary flow for a medium Prandtl number ($Pr = 6.7$) in rotating annular pools with different aspect ratios, showing that all instabilities are hydrothermal. Liu *et al.*[12] have studied thermocapillary flow instabilities in annular pools with different aspect ratios using both linear stability analysis and energy analysis, reporting that the instability mechanism in cases of a small Prandtl number ($Pr = 0.011$) is hydrodynamic, while for a medium Prandtl number ($Pr = 1.4$), it is influenced by both hydrodynamic and Marangoni effects.

On the other hand, thermocapillary effect induced by the axial temperature gradient also has a significant impact on the stability of jet flow. Xu and Davis[13] have investigated the stability of an infinitely long axisymmetric liquid column with interfacial deformation under such a gradient. They have found a new type of instability known as

the hydrothermal instability, in addition to the previously identified capillary instability[14] and surface-wave instability.[15] Furthermore, they have demonstrated that in simplified isothermal jets (the Biot number $Bi \to \infty$), the surface-wave instabilities may eradicate completely the tendency for capillary breakup. Similarly, the capillary breakup can be retarded or even suppressed for a small Prandtl number ($Pr < 1$) and a large Biot number ($Bi \geq 1$). Subsequent studies on annular liquid films[16] and encapsulated liquid floating zones[17] have further shown that the thermocapillary-driven flow within the liquid column significantly weakens the capillary instability, thereby enhancing the jet stability.

Wanschura *et al.*[18] have conducted linear stability analysis and energy analysis to investigate thermocapillary flow in a cylindrical liquid bridge with different *Pr*. They have found that the low Prandtl number instability is an instability of the basic axial shear flow, whereas the instability at high *Pr* is attributed to the convective radial heat transport coupled with the Marangoni effect. In a separate study, Levenstam and Amberg[19] have numerically simulated a half-zone model and determined that the instability at low *Pr* is purely hydrodynamic. Later, these findings were further supported by Leypoldt *et al.*[20] Recently, thermocapillary flows in liquid bridges between coaxial disks of unequal radii ratios have been widely examined.[21–23] Based on the methods of linear stability analysis and energy analysis, these studies have revealed that the instability modes at small *Pr* are primarily driven by hydrodynamic effects, while the instability mechanism at larger *Pr* cannot neglect the influence of thermocapillary effect.

Most previous studies have predominantly concentrated on understanding the mechanism of thermocapillary instabilities in liquid columns of finite volume. However, there is still limited investigations on long liquid columns, where the destabilization mechanism of unstable modes and the factors inhibiting capillary breakup remain unclear. Expanding upon the study conducted by Xu and Davis,[13] the present work explores the energy mechanism for the instability of liquid jets with thermocapillarity, presenting the perturbation flow fields and providing insight into the mechanisms that prevent the capillary breakup of jets.

The paper is organized as follows: Sec. II recalls the model of thermocapillary liquid jets, including dimensionless governing equations and boundary conditions, along with the basic state of flow and temperature profiles. Section III constructs the equation for perturbation kinetic energy. The results of energy components and relevant discussion are presented. Section IV is devoted to the analysis of perturbation fields and an explanation for the mechanism that suppresses capillary breakup. Finally, in Sec. V, we itemize the conclusions.

II. MATHEMATICAL FORMULATION

We consider an infinitely long liquid column of basic radius a with a deformable free surface $r = R(\theta, z, t)$, as illustrated in Fig. 1. The column is described using a cylindrical coordinate system (r, θ, z); the corresponding velocity components are (u, v, w). A temperature gradient $\mathrm{d}T/\mathrm{d}z = -b < 0$ is applied along the axial direction of the liquid column, while the surface tension σ varies linearly with the temperature,

$$\sigma = \sigma_0 - \gamma(T - T_0), \tag{1}$$

where T_0 is the temperature on the surface at $z = 0$, and $\gamma = -\mathrm{d}\sigma/\mathrm{d}T > 0$ is the rate of change in surface tension with respect to the temperature.

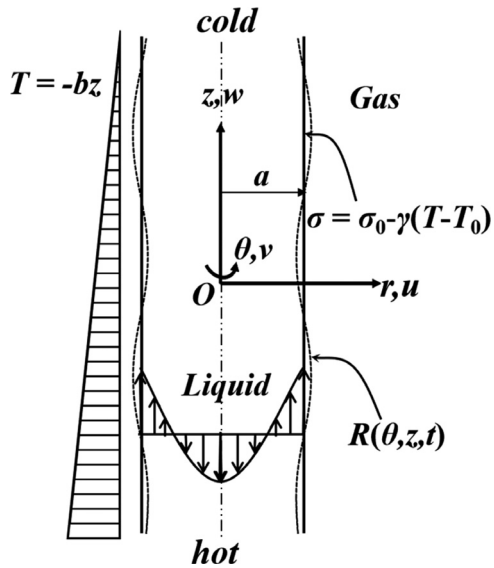

FIG. 1. The sketch of a basic-state liquid jet with thermocapillarity.

We consider an incompressible Newtonian fluid, whose dynamic viscosity μ, density ρ, specific heat c_p, thermal conductivity rate χ, and unit thermal surface conductance h are constants. Length $L \sim a$, velocity $\mathbf{u} \sim w_* = \gamma ba/\mu$, velocity $\mathbf{u} \sim w_{**} = (\sigma_0/\rho a)^{\frac{1}{2}}$, time $t \sim (\rho a^3/\sigma_0)^{\frac{1}{2}}$, pressure $p \sim \sigma_0/a$, temperature difference $T - T_0 \sim ba$, and surface tension $\sigma \sim \sigma_0$ are selected as characteristic scales. Here, the characteristic velocity w_{**} is related to the capillary instability, whereas w_* is consistent with the thermocapillary effect. This particular configuration considers both the capillary breakup and the thermocapillary effect in a long jet.

The following dimensionless numbers are generated:

$$S = \frac{\rho a \sigma_0}{\mu^2}, \quad R_{\mathrm{B}} = \frac{\rho \gamma b a^2}{\mu^2}, \quad Pr = \frac{\mu c_p}{\chi}, \quad Bi = \frac{ha}{\chi}. \tag{2}$$

Here, $S^{\frac{1}{2}}$ is the Reynolds number for the capillary instability, which is associated with mean surface tension.[13] R_{B} is the Reynolds number for the steady thermocapillary flow. *Pr* is the Prandtl number, and *Bi* is the surface Biot number that measures the heat transfer between the liquid and the surrounding gas.

A. Governing equations

In a cylindrical coordinate system, the mathematical model is expressed by the following dimensionless governing equations:

$$\nabla \cdot \mathbf{u} = 0, \tag{3a}$$

$$\partial_t \mathbf{u} + \mathbf{u} \cdot \nabla \mathbf{u} = -\nabla p + S^{-\frac{1}{2}} \nabla \cdot \boldsymbol{\tau}, \tag{3b}$$

$$Pr(\partial_t T + \mathbf{u} \cdot \nabla T) = S^{-\frac{1}{2}} \nabla^2 T. \tag{3c}$$

Here, $\mathbf{u}$, p, T, and $\boldsymbol{\tau}$ stand for the velocity, pressure, temperature, and stress tensor, respectively.

For Newtonian fluids,

$$\boldsymbol{\tau} = \dot{\boldsymbol{\gamma}}, \tag{4}$$

where $\dot{\boldsymbol{\gamma}} = \nabla \mathbf{u} + (\nabla \mathbf{u})^{\mathrm{T}}$.

The boundary conditions are listed as follows. At $r = 0$, all physical quantities must be finite values:

$$|u|, |v|, |w|, |p|, |T| < \infty. \tag{5}$$

On the liquid surface at $r = R(\theta, z, t)$,

$$\partial_t R + \mathbf{u}_\perp \cdot \nabla R = u, \tag{6}$$

$$\mathbf{t}_j \cdot \boldsymbol{\tau} \cdot \mathbf{n} = -S^{-\frac{1}{2}} R_\mathrm{B} \nabla T \cdot \mathbf{t}_j, \tag{7}$$

$$-p + S^{-\frac{1}{2}} \mathbf{n} \cdot \boldsymbol{\tau} \cdot \mathbf{n} = K(1 - Ca\, T), \tag{8}$$

$$-\nabla T \cdot \mathbf{n} = Bi(T - T_a). \tag{9}$$

Here, $j = 1, 2$, $\nabla f = \left(\partial_r f, \frac{1}{r}\partial_\theta f, \partial_z f\right)$, and f denotes a scalar. $\mathbf{u}_\perp = (v, w)$ represents a projection of $\mathbf{u}$ on the $\theta - z$ orthogonal face. The unit normal vector $\mathbf{n}$ and unit tangent vectors $\mathbf{t}_1$ and $\mathbf{t}_2$ at any point on the interface are given by

$$\mathbf{n} = \frac{1}{\sqrt{E}}\left(1, -\frac{1}{R}R_\theta, -R_z\right), \tag{10a}$$

$$\mathbf{t}_1 = \frac{1}{\sqrt{(1 + R_z^2)E}}\left(\frac{1}{R}R_\theta, 1 + R_z^2, -\frac{1}{R}R_\theta R_z\right), \tag{10b}$$

$$\mathbf{t}_2 = \frac{1}{\sqrt{1 + R_z^2}}(R_z, 0, 1), \tag{10c}$$

$$E = 1 + \frac{1}{R^2}{R_\theta}^2 + R_z^2. \tag{10d}$$

The curvature K is defined as

$$\begin{aligned} K = -\nabla \cdot \mathbf{n} &= -\left(\frac{1}{r}\frac{\partial(rn_1)}{\partial r} + \frac{1}{r}\frac{\partial(n_2)}{\partial \theta} + \frac{\partial(n_3)}{\partial z}\right) \\ &= \left[R^2(1 + R_z^2) + {R_\theta}^2\right]^{-\frac{3}{2}}\{RR_{zz}(R^2 + {R_\theta}^2) \\ &\quad - (1 + R_z^2)(R^2 - RR_{\theta\theta}) - 2RR_\theta R_z R_{\theta z} - 2{R_\theta}^2\}, \end{aligned} \tag{11}$$

where the subscript represents the partial derivative. $Ca = S^{-1}R_\mathrm{B}$ denotes the capillary number. T_a is the gas temperature near the interface.

Equation (6) shows the kinematic boundary condition, guaranteeing that the gas–liquid interface is smooth. Equation (7) indicates that the shear stress is balanced with the surface tension gradient generated by the thermocapillary effect. Equation (8) shows the stress balance in the normal direction. Equation (9) stands for the continuity of heat flux cross the liquid surface.

When the capillary number Ca satisfies

$$Ca = S^{-1}R_\mathrm{B} \ll 1, \tag{12}$$

the jet can be approximated as a parallel flow with perfectly cylindrical interface. We assume that the basic temperature exhibits a linear distribution in the z-direction,

$$\bar{\mathbf{u}} = (0, 0, \bar{w}(r)), \quad \bar{T}(r, z) = -z + \overline{T_b}(r). \tag{13}$$

Here, the superscript line denotes the basic flow, and $\overline{T_b}$ represents the radial temperature distribution. Therefore, the approximate solution of basic flow is determined as follows:[13]

$$(\bar{u}, \bar{v}) \approx 0, \tag{14a}$$

$$\bar{w} \approx \frac{1}{2}S^{-\frac{1}{2}}R_\mathrm{B}\left(r^2 - \frac{1}{2}\right), \tag{14b}$$

$$\bar{T} \approx -z - \frac{1}{32}PrR_\mathrm{B}(1 - r^2)^2, \tag{14c}$$

$$T_a \approx -z, \tag{14d}$$

$$\bar{p} \approx 1 + 2Ca\, z, \tag{14e}$$

$$R \approx 1, \tag{14f}$$

$$\bar{\boldsymbol{\tau}} \approx \partial_r \bar{w}(r)\begin{bmatrix} 0 & 0 & 1 \\ 0 & 0 & 0 \\ 1 & 0 & 0 \end{bmatrix}. \tag{14g}$$

Next, the stability of the flow is investigated by the modal analysis. A small disturbance in the normal mode form is superimposed on the basic flow,

$$\begin{aligned} (\mathbf{u}, T, p, \boldsymbol{\tau}, R) = \left(\bar{\mathbf{u}}, \bar{T}, \bar{p}, \bar{\boldsymbol{\tau}}, 1\right) + \mathrm{Re}\Big\{\Big(\hat{\mathbf{u}}(r), \hat{T}(r), \hat{p}(r), \hat{\boldsymbol{\tau}}(r), \hat{\xi}\Big) \\ \times \exp\left[\sigma t + i(\alpha z + m\theta)\right]\Big\}. \end{aligned} \tag{15}$$

Here, the variables without superscript line stand for the perturbation. The eigenvalue $\sigma = \sigma_r + \mathrm{i}\sigma_i$ consists of the growth rate σ_r and frequency σ_i. α denotes the axial wavenumber, and the integer m represents the azimuthal wavenumber.

Substituting Eq. (15) in the fundamental equations and linearizing the equations with respect to the perturbation quantities, we can derive that

$$\hat{u} + r\mathrm{D}\hat{u} + \mathrm{i}m\hat{v} + \mathrm{i}\alpha r\hat{w} = 0, \tag{16}$$

$$\mathrm{i}m\hat{\tau}_{12} + \mathrm{i}\alpha r\hat{\tau}_{13} + r\mathrm{D}\hat{\tau}_{11} + \hat{\tau}_{11} - \hat{\tau}_{22} - S^{\frac{1}{2}}\mathrm{i}\alpha r\bar{w}\hat{u} = S^{\frac{1}{2}}r\mathrm{D}\hat{p} + \sigma S^{\frac{1}{2}}r\hat{u}, \tag{17a}$$

$$\mathrm{i}m\hat{\tau}_{22} + \mathrm{i}\alpha r\hat{\tau}_{23} + r\mathrm{D}\hat{\tau}_{12} + 2\hat{\tau}_{12} - S^{\frac{1}{2}}\mathrm{i}\alpha r\bar{w}\hat{v} = S^{\frac{1}{2}}\mathrm{i}m\hat{p} + \sigma S^{\frac{1}{2}}r\hat{v}, \tag{17b}$$

$$\begin{aligned} &\mathrm{i}m\hat{\tau}_{23} + \mathrm{i}\alpha r\hat{\tau}_{33} + r\mathrm{D}\hat{\tau}_{13} + \hat{\tau}_{13} - S^{\frac{1}{2}}r\mathrm{D}\bar{w}\hat{u} - S^{\frac{1}{2}}\mathrm{i}\alpha r\bar{w}\hat{w} \\ &\quad = S^{\frac{1}{2}}\mathrm{i}\alpha r\hat{p} + \sigma S^{\frac{1}{2}}r\hat{w}, \end{aligned} \tag{17c}$$

$$\begin{aligned} &\left\{r^2\mathrm{D}^2 + r\mathrm{D} - \alpha^2 r^2 - m^2 - PrS^{\frac{1}{2}}\mathrm{i}\alpha r^2\bar{w}\right\}\hat{T} - PrS^{\frac{1}{2}}r^2(\mathrm{D}\bar{T}\hat{u} + \bar{T}_z\hat{w}) \\ &\quad = \sigma PrS^{\frac{1}{2}}r^2\hat{T}, \end{aligned} \tag{18}$$

where $\mathrm{D} \equiv \partial_r$ denotes the partial derivative with respect to r. Following Chaudhary *et al.*,[24] Eqs. (17) are written in a general form represented by the perturbation stress, which can extend to non-Newtonian fluids.

The linear perturbation constitutive equation for a Newtonian fluid is

$$\begin{cases} \hat{\tau}_{11} - 2\mathrm{D}\hat{u} = 0, \quad r\hat{\tau}_{12} - \mathrm{i}m\hat{u} - r\mathrm{D}\hat{v} + \hat{v} = 0, \\ \hat{\tau}_{13} - \mathrm{i}\alpha\hat{u} - \mathrm{D}\hat{w} = 0, \quad r\hat{\tau}_{22} - 2(\mathrm{i}m\hat{v} + \hat{u}) = 0, \\ r\hat{\tau}_{23} - \mathrm{i}\alpha r\hat{v} - \mathrm{i}m\hat{w} = 0, \quad \hat{\tau}_{33} - 2\mathrm{i}\alpha\hat{w} = 0. \end{cases} \tag{19}$$

The linear perturbation boundary conditions are written as follows. At the center axis $r = 0$,[25]

$$\begin{cases} m=0: \hat{u}=0, \quad \hat{v}=0, \quad \mathrm{D}\hat{w}=0, \quad \mathrm{D}\hat{T}=0; \\ m=1: \mathrm{D}\hat{u}=0, \quad \hat{u}+\mathrm{i}\hat{v}=0, \quad \hat{w}=0, \quad \hat{T}=0; \\ m>1: \hat{u}=0, \quad \hat{v}=0, \quad \hat{w}=0, \quad \hat{T}=0. \end{cases} \tag{20}$$

On the liquid surface at $r=1$,

$$\hat{u}-\mathrm{i}\alpha\bar{w}\hat{\xi}=\sigma\hat{\xi}, \tag{21}$$

$$\hat{\tau}_{12}+S^{-\frac{1}{2}}R_{\mathrm{B}}\mathrm{i}m\left(2\mathrm{D}\bar{T}\hat{\xi}+\hat{T}\right)=0, \tag{22}$$

$$\mathrm{D}\bar{\tau}_{13}\hat{\xi}+\hat{\tau}_{13}+S^{-\frac{1}{2}}R_{\mathrm{B}}\mathrm{i}\alpha\left(2\mathrm{D}\bar{T}\hat{\xi}+\hat{T}\right)=0, \tag{23}$$

$$-\hat{p}+S^{-\frac{1}{2}}\left(\hat{\tau}_{11}-2\mathrm{i}\alpha\bar{\tau}_{13}\hat{\xi}\right)-\left(1-\alpha^2-m^2\right)\hat{\xi}-Ca\left(\mathrm{D}\bar{T}\hat{\xi}+\hat{T}\right)=0, \tag{24}$$

$$Bi\left(\hat{T}+\mathrm{D}\bar{T}\hat{\xi}\right)+\mathrm{D}\hat{T}+\left(\mathrm{D}^2\bar{T}-\mathrm{i}\alpha\bar{T}_z\right)\hat{\xi}=0. \tag{25}$$

The normal stress boundary condition (24) requires that the surface tension does not vary much over the characteristic axial wavelength of the disturbance, i.e.,

$$Ca\cdot 2\pi/\alpha \ll 1, \tag{26}$$

thus, $(1-Ca\,\bar{T}(z,1))(1-\alpha^2-m^2)\hat{\xi}\approx(1-\alpha^2-m^2)\hat{\xi}$, where $\bar{T}(z,1)=-z$.

We can use the Chebyshev collocation method to solve the general eigenvalue problem expressed as $Wg=\sigma Zg$, where W and Z are two matrices, and g is the eigenvector. Before solving the equations, $\hat{p}$ in Eqs. (17) and (24) can be eliminated. The details on this process can be found in Appendix A. N_c Gauss–Lobatto points are set for the governing equations in the flow region $r=(1-\cos(\frac{j\pi}{N_c+1}))/2$, $j=1\sim N_c$, and two extra points are set for the boundary conditions at $r=0,1$.

Table I presents the eigenvalues of the neutral capillary mode calculated by using different numbers of collocation points. We choose 70–80 collocation points for our numerical solution, balancing the accuracy and the efficiency. Xu and Davis[13] have given an approximate expression (6–2) that describes the dispersion relation for a non-isothermal jet when α is small. Table II presents a comparison of the eigenvalues obtained by Xu and Davis (XD) with those calculated in our present study (PW). The relative errors are less than 2.5×10^{-2}, confirming the dependability of our computational findings.

III. ENERGY ANALYSIS

The rate of change of perturbation kinetic energy is given by[17]

TABLE I. The eigenvalues of neutral capillary mode computed by different numbers of collocation points at $Bi=1$, $Pr=0.1$, $R_{\mathrm{B}}=200$, $S=10^4$, $\alpha=0.864$, and $m=0$.

N_c	σ_r ($\times10^{-4}$)	σ_i ($\times10^{-2}$)
30	4.179 40	4.843 199 3
50	4.179 40	4.843 199 3
80	4.179 40	4.843 199 3
100	4.179 40	4.843 199 4

TABLE II. A comparison of eigenvalues for the non-isothermal case at $Bi=1$, $Pr=0.1$, $R_{\mathrm{B}}=10$, and $S=10^2$. Here, "XD" and "PW" stand for the results of Xu and Davis and the present work, respectively.

α	XR	PW
0.01	0.022 36 + 0.022 11i	0.022 86 + 0.021 61i
	−0.022 36 − 0.022 61i	−0.022 89 − 0.022 11i
0.001	0.007 07 + 0.007 05i	0.007 06 + 0.007 03i
	−0.007 07 − 0.007 10i	−0.007 06 − 0.007 08i

$$\begin{aligned}\partial_t E_k &= -\frac{1}{2}S^{-\frac{1}{2}}\int(\boldsymbol{\tau}:\dot{\boldsymbol{\gamma}})\mathrm{d}^3r+S^{-\frac{1}{2}}\int(\mathbf{u}\cdot\boldsymbol{\tau}\cdot\mathbf{n})\mathrm{d}^2r \\ &\quad -\int\mathbf{u}\cdot((\mathbf{u}\cdot\nabla)\bar{\mathbf{u}})\mathrm{d}^3r-\int(p\mathbf{u}\cdot\mathbf{n})\mathrm{d}^2r \\ &= -N+M+I+P_S.\end{aligned} \tag{27}$$

Here, $E_k=\frac{1}{2}\int|\mathbf{u}|^2\mathrm{d}^3r$, whose integral area is $0\le r\le1$, $0\le\theta\le2\pi$, $0\le z\le2\pi/\alpha$.

$\int f\mathrm{d}^3r$ and $\int f\mathrm{d}^2r$ represent volume integral and surface integral, respectively. N is the work done by stress in the bulk of the jet, M is the work done by the stress on the surface, I is the energy from the basic flow, and P_S is the work done by the pressure on the surface. For Newtonian fluids, Eq. (18) indicates that $N>0$, meaning that viscous dissipation always occurs in the liquid column, the same as the liquid layer.[26,27] The perturbation energy is normalized as $\int|\mathbf{u}|^2\mathrm{d}^3r=1$ in the following.

On the deformable surface, there are horizontal and vertical components for the stress. As a result, M can be decomposed into two following terms:[28]

$$M=S^{-\frac{1}{2}}\int u\tau_{11}\mathrm{d}^2r+S^{-\frac{1}{2}}\int(v\tau_{12}+w\tau_{13})\mathrm{d}^2r=M_v+M_h. \tag{28}$$

Here, M_v and M_h represent the work done by vertical and horizontal components of the stress, respectively. According to boundary conditions (21) and (22), the perturbed shear stress on the surface can be caused by both the thermocapillary effect and interfacial deformation. Therefore, M_h can be further decomposed into two parts as follows:

$$M_h=M_{hT}+M_{hR}, \tag{29a}$$

$$M_{hT}=-S^{-1}R_{\mathrm{B}}\int\left(v\frac{\partial T}{\partial\theta}+w\frac{\partial T}{\partial z}\right)\mathrm{d}^2r, \tag{29b}$$

$$\begin{aligned}M_{hR}&=-2S^{-1}R_{\mathrm{B}}\int v\mathrm{D}\bar{T}\frac{\partial\xi}{\partial\theta}\,\mathrm{d}^2r \\ &\quad -S^{-\frac{1}{2}}\int w\left(\mathrm{D}\bar{\tau}_{13}\xi+2S^{-\frac{1}{2}}R_{\mathrm{B}}\mathrm{D}\bar{T}\frac{\partial\xi}{\partial z}\right)\mathrm{d}^2r.\end{aligned} \tag{29c}$$

Here, M_{hT} and M_{hR} stand for the work done by thermocapillary force and interfacial deformation-induced shear stress, respectively.

This paper uses the terminology suggested by Xu and Davis[13] to label the capillary mode, surface-wave mode, and hydrodynamic mode with azimuthal wavenumber $m=0$ as $W_0^{(c)}$, $W_0^{(-)}$, and $W_0^{(+)}$, respectively. When the dispersion relations of the capillary mode and surface wave mode are connected in a curve, α_{B} is the wave number corresponding to the transition point of the two modes. The capillary

mode $W_0^{(c)}$ is for $\alpha < \alpha_B$, and surface-wave mode $W_0^{(-)}$ is for $\alpha > \alpha_B$. Xu and Davis[13] have also found that for isothermal jets (axial wavenumber α approximately less than 2) or non-isothermal jets, some unstable modes $m = 0$ become the most dangerous mode. In some cases, the increase in R_B can suppress the unstable capillary modes. In order to comprehend the underlying energy mechanism, we conduct the energy analysis on the capillary mode $W_0^{(c)}$, surface-wave mode $W_0^{(-)}$, and hydrodynamic mode $W_0^{(+)}$.

A. The "flying jet"

When $Bi \to \infty$, we can obtain from Eq. (25) that $T(1) = 0$, and there are no temperature perturbations on the free surface. Therefore, all unstable modes are actually isothermal and independent of Pr. The basic temperature field is important only in that the thermocapillary force drives the basic flow, which can be considered as driven by the "wind stress" having the same magnitude as the thermocapillary gradient γb. This situation is referred to as the isothermal "flying jet" by Xu and Davis.[13] Thus, R_B serves as the Reynolds number of the flying jet. Such isothermal cases do not require the "slowly varying" approximation, i.e., Eq. (26).[29] Therefore, all physical modes need only satisfy the constraint (12). In these cases, the dispersion curves of the capillary mode $W_0^{(c)}$ and surface-wave mode $W_0^{(-)}$ are connected smoothly.

Tables III and IV present the terms of the perturbation energy growth for the isothermal jet for the capillary mode $W_0^{(c)}$, surface-wave mode $W_0^{(-)}$, and hydrodynamic mode $W_0^{(+)}$ at $\alpha = 0.4 < \alpha_B$, $S = 10^4$. Tables V and VI present the cases for the isothermal jet for surface-wave mode $W_0^{(-)}$ and hydrodynamic mode $W_0^{(+)}$ at $\alpha = 1.4 > \alpha_B$ and $S = 10^4$. It is evident that thermocapillary forces do no work ($M_{hT} = 0$), which is obvious in the isothermal case.

For $0 < \alpha < \alpha_B$, N is the viscous dissipating in the capillary mode $W_0^{(c)}$ and hydrodynamic mode $W_0^{(+)}$. P_S is the main energy dissipation for the stable hydrodynamic mode $W_0^{(+)}$, but the main energy source in the unstable capillary mode $W_0^{(c)}$. When P_S significantly decreases with R_B, the capillary mode $W_0^{(c)}$ is stabilized. For $\alpha > \alpha_B$, P_S, M and I serve as energy sources, while N is the only pathway of energy dissipation for the surface-wave mode $W_0^{(-)}$. For the hydrodynamic mode $W_0^{(+)}$, P_S is still the energy source, while N and I dissipate the energy. The sign of M depends on the parameters.

The physical reason for these phenomena can be explained as follows. In the inviscid jet [$R_B = O(1)$ as $S \to \infty$],[13] $N = M = I = 0$ in Eq. (27), suggesting that P_S is the main energy source for the unstable

TABLE III. The terms of the perturbation energy growth for the isothermal jet for the capillary mode $W_0^{(c)}$ and the surface-wave mode $W_0^{(-)}$ at $\alpha = 0.4$ and $S = 10^4$.

Mode	$W_0^{(c)}$			$W_0^{(-)}$
R_B	100	200	300	500
α_B	0.9439	0.8175	0.5158	0.2140
$\partial_t E_k$	0.237 63	0.180 71	0.046 31	−0.011 07
P_S	0.229 42	0.148 78	0.024 52	0.000 71
$-N$	−0.005 99	−0.009 40	−0.013 40	−0.007 00
I	0.004 66	0.012 08	−0.007 82	−0.030 30
M	0.009 54	0.029 25	0.043 01	0.025 51
M_{hR}	0.007 83	0.027 14	0.040 52	0.023 65
M_{hT}	0.000 00	0.000 00	0.000 00	0.000 00
M_v	0.001 71	0.002 11	0.002 49	0.001 86

TABLE IV. The terms of the perturbation energy growth for the isothermal jet for the hydrodynamic mode $W_0^{(+)}$ at $\alpha = 0.4$ and $S = 10^4$.

Mode	$W_0^{(+)}$			
R_B	100	200	300	500
$\partial_t E_k$	−0.237 03	−0.195 20	−0.114 06	−0.059 77
P_S	−0.242 32	−0.204 49	−0.153 39	−0.203 45
$-N$	−0.012 50	−0.030 22	−0.043 36	−0.154 02
I	0.010 11	0.009 47	0.006 58	0.032 45
M	0.007 68	0.030 04	0.076 10	0.265 25
M_{hR}	0.005 68	0.027 36	0.072 94	0.261 00
M_{hT}	0.000 00	0.000 00	0.000 00	0.000 00
M_v	0.001 99	0.002 68	0.003 17	0.004 24

TABLE V. The terms of the perturbation energy growth for the isothermal jet for the surface-wave mode $W_0^{(-)}$ at $\alpha = 1.4 > \alpha_B$ and $S = 10^4$.

Mode	$W_0^{(-)}$			
R_B	100	200	300	500
α_B	0.9439	0.8175	0.5158	0.2140
$\partial_t E_k$	−0.012 09	−0.000 45	0.006 08	0.010 91
P_S	0.004 56	0.006 55	0.009 44	0.013 03
$-N$	−0.058 71	−0.059 66	−0.060 26	−0.060 84
I	0.011 02	0.014 95	0.015 72	0.014 53
M	0.031 03	0.037 70	0.041 18	0.044 19
M_{hR}	0.010 73	0.016 45	0.019 44	0.022 00
M_{hT}	0.000 00	0.000 00	0.000 00	0.000 00
M_v	0.020 31	0.021 25	0.021 74	0.022 19

TABLE VI. The terms of the perturbation energy growth for the isothermal jet for the hydrodynamic mode $W_0^{(+)}$ at $\alpha = 1.4$ and $S = 10^4$.

Mode	$W_0^{(+)}$			
R_B	100	200	300	500
$\partial_t E_k$	−0.047 23	−0.063 10	−0.075 20	−0.091 14
P_S	0.039 66	0.113 27	0.245 46	0.663 77
$-N$	−0.058 68	−0.067 94	−0.096 90	−0.263 21
I	−0.026 23	−0.081 02	−0.178 68	−0.516 14
M	−0.001 97	−0.027 40	−0.045 08	0.024 44
M_{hR}	−0.017 42	−0.038 23	−0.050 16	0.030 20
M_{hT}	0.000 00	0.000 00	0.000 00	0.000 00
M_v	0.015 44	0.010 84	0.005 09	−0.005 76

TABLE VII. The terms of perturbation energy growth for the most unstable modes at $S = 10^4$.

Mode	R_B	α_M	$\partial_t E_k$	P_S	$-N$	I	M	M_{hR}	M_{hT}	M_v
$W_0^{(c)}$	0	0.690	0.3363	0.3457	−0.0138	0.0000	0.0045	0.0000	0.0000	0.0045
	100	0.654	0.3015	0.2928	−0.0143	0.0075	0.0156	0.0110	0.0000	0.0046
	200	0.532	0.1989	0.1643	−0.0138	0.0138	0.0346	0.0308	0.0000	0.0038
	300	0.273	0.0646	0.0330	−0.0100	0.0018	0.0399	0.0387	0.0000	0.0012
	500	0.051	0.0241	0.0024	−0.0051	−0.0002	0.0270	0.0270	0.0000	0.0000
$W_0^{(-)}$	200	1.051	0.0084	0.0082	−0.0344	0.0008	0.0337	0.0214	0.0000	0.0123
	300	1.141	0.0096	0.0091	−0.0403	0.0050	0.0358	0.0213	0.0000	0.0145
	500	1.302	0.0112	0.0122	−0.0526	0.0104	0.0412	0.0221	0.0000	0.0191

capillary mode $W_0^{(c)}$. This mechanism still keeps in the flying jet. For the hydrodynamic mode $W_0^{(+)}$ at $S = 10^4$, it can be seen from Eq. (24) that $-\hat{p}(1) \approx (1-\alpha^2)\hat{\xi}$. The phase difference between the $\hat{p}(1)$ and $\hat{\xi}$ at $\alpha < 1$ is opposite to that at $\alpha > 1$, while the phase difference between $\hat{u}$ and $\hat{\xi}$ is not very sensitive to α. As a result, the sign of P_S is different in these two cases of $W_0^{(+)}$. The surface-wave mode $W_0^{(-)}$ is caused by the "wind stress,"[29] so the work done by the stress on the surface (M) is crucial for $W_0^{(-)}$.

In Table III, the growth rate of perturbation energy for the capillary mode $W_0^{(c)}$ gradually decreases with R_B. The explanation is given in the last part of Sec. IV A. However, the case is opposite for the surface-wave mode $W_0^{(-)}$ in Table V. The reason is that $W_0^{(-)}$ is caused by the wind stress, whose magnitude can be measured by R_B. This indicates that the velocity distribution in Eq. (14b) caused by the wind stress[29] can suppress capillary instabilities, allowing for longer continuous jets, but trigger surface-wave instabilities.

Table VII displays the perturbation energy growth for the most unstable modes at $S = 10^4$, where α_M is the corresponding wavenumber. As R_B increases, the perturbation energy growth decreases for the capillary mode $W_0^{(c)}$, while the opposite occurs for the surface-wave mode $W_0^{(-)}$, in agreement with the preceding analysis. It should be noted that for $R_B \geq 200$, both $W_0^{(c)}$ and $W_0^{(-)}$ are unstable. However, the growth rates of $W_0^{(c)}$ and $W_0^{(-)}$ are smaller than those of the capillary mode $W_0^{(c)}$ at $R_B = 0$ and $R_B = 100$. Therefore, the increase in R_B can still slow down the process of capillary breakup, extending the jet zone.

TABLE VIII. The terms of the perturbation energy growth for the capillary mode $W_0^{(c)}$ at $R_B = 100$, $\alpha = 0.4$, and $S = 10^4$.

$W_0^{(c)}$	$Bi \to \infty$	$Bi = 100$ $Pr = 0.1$	$Bi = 1$ $Pr = 0.1$	$Bi = 1$ $Pr = 0.5$
$\partial_t E_k$	0.237 63	0.237 58	0.234 97	0.232 20
P_S	0.229 42	0.229 57	0.236 87	0.243 12
$-N$	−0.005 99	−0.005 95	−0.004 79	−0.004 94
I	0.004 66	0.004 59	0.001 09	0.000 14
M_{hR}	0.007 83	0.007 80	0.006 49	0.005 92
M_{hT}	0.000 00	−0.000 13	−0.006 25	−0.013 42
M_v	0.001 71	0.001 71	0.001 57	0.001 37

B. Thermocapillary instabilities

When Bi is finite, the jet becomes non-isothermal, both restrictions (12) and (26) should be satisfied for the physical modes.[13] If $R_B \neq 0$, thermocapillary forces become the driving force for the surface flow.

Xu and Davis[13] have suggested that the modes $m = 0$ at large Bi ($Bi \geq 1$) and small Pr ($Pr < 1$) are similar to those in the isothermal cases. Table VIII shows the terms of the perturbation energy growth for the capillary mode $W_0^{(c)}$ at $R_B = 100$, $\alpha = 0.4$, and $S = 10^4$. It can be seen that for unstable capillary modes $W_0^{(c)}$, P_S is dominant and changes little. Thus, their energy mechanisms are also similar.

1. The effect of R_B

For large Bi ($Bi \geq 1$) and small Pr ($Pr < 1$), as R_B increases, the capillary mode $W_0^{(c)}$ and surface-wave mode $W_0^{(-)}$ split. In addition, when R_B is not large, the surface-wave mode $W_0^{(-)}$ generates a new branch $W_0^{(-)'}$, and the hydrodynamic mode $W_0^{(+)}$ also has a new branch $W_0^{(+)'}$. As R_B increases, the branch $W_0^{(-)'}$ disappears, while branch $W_0^{(+)'}$ becomes more stable (see Figs. 6 and 7 in Ref. 13).

Tables IX and X show the terms of the perturbation energy growth of the non-isothermal jet for the modes $W_0^{(c)}$ and $W_0^{(+)}$, respectively. In Table IX, when R_B is small, the capillary mode $W_0^{(c)}$ mainly absorbs energy from P_S. However, as R_B increases, the energy

TABLE IX. The terms of the perturbation energy growth for the non-isothermal jet for the capillary mode $W_0^{(c)}$ at $\alpha = 0.6$, $Pr = 0.1$, $Bi = 1$, and $S = 10^4$.

Mode	$W_0^{(c)}$			
R_B	40	100	200	300
$\partial_t E_k$	0.321 77	0.294 12	0.181 26	0.013 89
P_S	0.328 80	0.298 84	0.157 17	−0.002 80
$-N$	−0.010 52	−0.010 63	−0.013 70	−0.044 51
I	0.000 22	0.002 30	0.014 03	−0.040 33
M	0.003 27	0.003 61	0.023 76	0.101 53
M_{hR}	0.001 35	0.008 51	0.032 12	0.051 67
M_{hT}	−0.001 50	−0.008 33	−0.012 70	0.042 80
M_v	0.003 42	0.003 43	0.004 34	0.007 05

TABLE X. The terms of the perturbation energy growth for the non-isothermal jet for the hydrodynamic mode $W_0^{(+)}$ at $\alpha = 0.6$, $Pr = 0.1$, $Bi = 1$, and $S = 10^4$.

Mode	$W_0^{(+)}$			
R_B	40	100	200	300
$\partial_t E_k$	−0.192 36	−0.201 02	−0.154 56	−0.094 43
P_S	−0.032 37	−0.188 37	−0.312 04	−0.361 33
$-N$	−0.167 42	−0.170 61	−0.189 79	−0.369 29
I	0.006 30	0.051 55	0.113 12	0.151 70
M	0.001 13	0.106 40	0.234 15	0.484 49
M_{hR}	−0.001 91	−0.006 61	0.009 82	−0.012 64
M_{hT}	0.002 96	0.109 65	0.217 53	0.490 55
M_v	0.000 08	0.003 36	0.006 81	0.006 57

contribution from P_S decreases rapidly. As a result, the rate of change of perturbation kinetic energy also decreases. When R_B further increases, M becomes the main energy source, while the other terms are dissipative. However, the growth rate of capillary mode $W_0^{(c)}$ largely decreases, and the flow becomes more stable. Table X indicates that the energy for hydrodynamic mode $W_0^{(+)}$ mainly comes from M_{hT}, but is dissipated by N and P_S. When R_B is large enough, M_{hT} dominates.

If Pr becomes larger, new unstable modes appear. Table XI shows the terms of the perturbation energy growth for the non-isothermal jet for the hydrodynamic mode $W_0^{(+)}$ at different R_B. It can be seen that when R_B increases, M_{hT} becomes dominant and $W_0^{(+)}$ becomes more unstable. It should be noted that $W_0^{(+)}$ gives rise to a new unstable mode known as the hydrothermal instability,[13] which exhibits a completely different energy mechanism compared to the unstable modes in isothermal conditions.

Table XII presents the energy growth for the non-isothermal jet for the surface-wave mode $W_0^{(-)}$ at $\alpha = 1.4$, $Pr = 0.1$, $Bi = 1$, and $S = 10^4$. It is found that the mode is dissipated by N and M_{hT}. As R_B increases, M_{hT} becomes more negative, N changes little, while other items increase. The growth rate of perturbation energy becomes positive, indicating the appearance of surface-wave instability.

Table XIII shows the perturbation energy growth for the non-isothermal jet for the new branch of surface-wave mode $W_0^{(-)'}$, the

TABLE XI. The terms of the perturbation energy growth for the non-isothermal jet for the hydrodynamic mode $W_0^{(+)}$ at $\alpha = 1$, $Pr = 5$, $Bi = 1$, and $S = 10^4$.

Mode	$W_0^{(+)}$			
R_B	40	100	200	300
$\partial_t E_k$	−0.003 55	0.026 67	0.072 83	0.115 87
P_S	−0.074 25	−0.081 02	−0.090 08	−0.097 19
$-N$	−0.318 96	−0.549 84	−0.861 76	−1.133 26
I	−0.013 03	−0.035 78	−0.066 88	−0.093 62
M_{hR}	−0.045 71	−0.054 71	−0.062 91	−0.068 47
M_{hT}	0.429 03	0.728 25	1.134 12	1.487 67
M_v	0.019 36	0.019 76	0.020 34	0.020 73

TABLE XII. The terms of the perturbation energy growth for the non-isothermal jet for the surface-wave mode $W_0^{(-)}$ at $\alpha = 1.4$, $Pr = 0.1$, $Bi = 1$, and $S = 10^4$.

Mode	$W_0^{(-)}$			
R_B	40	100	200	300
$\partial_t E_k$	−0.022 44	−0.012 71	0.001 67	0.011 58
P	0.009 98	0.010 82	0.014 22	0.018 00
$-N$	−0.057 13	−0.057 13	−0.057 66	−0.058 06
I	0.006 27	0.014 40	0.024 64	0.030 69
M	0.018 44	0.019 21	0.020 47	0.020 95
M_{hR}	0.004 91	0.010 19	0.015 44	0.018 19
M_{hT}	−0.004 81	−0.009 47	−0.013 99	−0.016 60
M_v	0.018 34	0.018 50	0.019 02	0.019 37

surface-wave mode $W_0^{(-)}$, and the capillary mode $W_0^{(c)}$. Figure 7 in Ref. 13 suggests that $W_0^{(-)'}$ gradually disappears as R_B increases. In Table XIII, the branch $W_0^{(-)'}$ at $R_B = 40$ and the surface-wave mode $W_0^{(-)}$ at $R_B = 100$ have similar values for each term. Hence, it is reasonable to infer that when R_B increases, the branch $W_0^{(-)'}$ at $0 < \alpha < \alpha_B$ becomes the surface-wave mode $W_0^{(-)}$, while the branch $W_0^{(-)'}$ at $\alpha > \alpha_B$ becomes the capillary mode $W_0^{(c)}$. As the branch of hydrodynamic mode $W_0^{(+)\prime}$ becomes more stable as R_B increases, its energy analysis is omitted.

Table XIV shows the energy mechanism for the most unstable modes at $Pr = 0.5$, $Bi = 1$ and $S = 10^4$. As R_B increases, $\partial_t E_k$ decreases for $W_0^{(c)}$, while the variation of $\partial_t E_k$ for $W_0^{(-)}$ is not monotonous. On the other hand, $\partial_t E_k$ of $W_0^{(+)}$ increases. This suggests that the appearance of surface-wave and hydrothermal instabilities suppress the capillary breakup and allow for a longer jet region. Although unstable capillary modes $W_0^{(c)}$ at $R_B = 350$ and 500 do not fully satisfy (26), the suppression of capillary instability still occurs.

TABLE XIII. The terms of the perturbation energy growth for the non-isothermal jet for the new branch of surface-wave mode $W_0^{(-)'}$ at $Pr = 0.1$, $Bi = 1$, $S = 10^4$, and $R_B = 40$ and the surface-wave mode $W_0^{(-)}$ and the capillary mode $W_0^{(c)}$ at $Pr = 0.1$, $Bi = 1$, $S = 10^4$, and $R_B = 100$.

Mode	$W_0^{(-)'}$	$W_0^{(-)}$	$W_0^{(-)'}$	$W_0^{(c)}$
R_B	40	100	40	100
α_B	0.9789	—	0.9789	—
α	$\alpha = 0.4 < \alpha_B$		$\alpha = 1.2 > \alpha_B$	
P_S	−0.004 98	−0.021 41	0.008 06	0.010 67
$-N$	−0.146 49	−0.131 83	−0.041 06	−0.041 06
I	0.004 58	0.011 58	0.005 55	0.012 47
M_{hR}	−0.001 08	−0.003 71	0.006 61	0.012 50
M_{hT}	0.000 51	0.010 58	−0.005 44	−0.010 40
M_v	−0.000 26	−0.000 96	0.012 82	0.012 89

TABLE XIV. The rate of change of perturbation energy for the most unstable modes at $Pr = 0.5$, $Bi = 1$, and $S = 10^4$.

Mode	R_B	α_M	$\partial_t E_k$	P_S	$-N$	I	M	M_{hR}	M_{hT}	M_v
$W_0^{(c)}$	40	0.683	0.3292	0.3416	−0.0135	−0.0004	0.0014	0.0014	−0.0042	0.0042
	100	0.649	0.2934	0.3088	−0.0126	0.0035	−0.0064	0.0091	−0.0189	0.0034
	200	0.574	0.1957	0.1519	−0.0175	0.0313	0.0299	0.0320	−0.0062	0.0041
	350	0.562	0.0814	−0.0045	−0.0818	−0.0193	0.1871	0.0576	0.1220	0.0075
	500	0.680	0.0546	−0.0453	−0.1915	−0.0663	0.3577	0.0693	0.2760	0.0124
$W_0^{(-)}$	100	1.015	0.0129	0.0207	−0.0287	0.0166	0.0044	0.0169	−0.0205	0.0079
	200	0.974	0.0288	0.0261	−0.0272	0.0303	−0.0004	0.0186	−0.0262	0.0073
	350	0.853	0.0414	0.0291	−0.0223	0.0434	−0.0089	0.0194	−0.0342	0.0058
	500	0.820	0.0373	0.0281	−0.0212	0.0422	−0.0118	0.0202	−0.0380	0.0060
$W_0^{(+)}$	350	1.547	0.0086	−0.3108	−0.8601	−0.0008	1.1803	−0.1390	1.2427	0.0767
	500	1.821	0.0418	−0.4490	−1.4131	0.0046	1.8993	−0.1630	1.9501	0.1123

TABLE XV. The terms of the perturbation energy growth for the non-isothermal jet for the capillary mode $W_0^{(c)}$ at $\alpha = 0.6$, $R_B = 300$, $Bi = 1$, and $S = 10^4$.

Mode	$W_0^{(c)}$		
Pr	1	5	10
$\partial_t E_k$	0.139 129	0.197 955	0.210 977
P_S	0.022 032	0.025 869	0.027 774
$-N$	−0.078 454	−0.124 960	−0.141 570
I	0.006 044	0.002 586	−0.005 104
M	0.189 507	0.294 459	0.329 876
M_{hR}	0.055 316	0.058 873	0.059 445
M_{hT}	0.125 715	0.226 050	0.260 630
M_v	0.008 476	0.009 536	0.009 801

2. *The effect of* Pr

For large Bi, as Pr increases, the capillary mode $W_0^{(c)}$ and surface-wave mode $W_0^{(-)}$ are also distinctly separated (see Figs. 11 and 12 in Ref. 13). Tables XV and XVI present the perturbation energy growth of the non-isothermal jet for the capillary mode $W_0^{(c)}$ and hydrodynamic mode $W_0^{(+)}$, respectively. In Table XV, as Pr increases, the energy dissipated by N increases and I changes from positive to negative. However, both P_S and M increase. The increase in $\partial_t E_k$ indicates that $W_0^{(c)}$ becomes more unstable.

In Table XVI, N is the main energy dissipation, while M_{hT} becomes the main energy source. Thus, $W_0^{(+)}$ belongs to the hydrothermal instability. In Tables XI and XVI, it can be found that the increase in R_B or Pr leads to the increase in M_{hT} and the hydrothermal instability. Therefore, if we define the Marangoni number as $Ma_B \equiv PrR_B$, then the increase in Ma_B can also lead to unstable hydrodynamic modes.

Table XVII presents the perturbation energy growth for the non-isothermal jet for the most unstable surface-wave modes $W_0^{(-)}$ at $R_B = 300$, $Bi = 1$, and $S = 10^4$. It can be seen that P_S, M_{hR}, and I are energy sources for $W_0^{(-)}$, while N and M_{hT} are dissipative. However, the growth rates of unstable modes in Table XVII are relatively small compared to those in Tables XV and XVI. Since the new branch of the hydrodynamic mode $W_0^{(+)'}$ remains stable, its energy analysis is omitted.

TABLE XVI. The terms of the perturbation energy growth for the non-isothermal jet for the hydrodynamic mode $W_0^{(+)}$ at $\alpha = 1$, $R_B = 300$, $Bi = 1$, and $S = 10^4$.

Mode	$W_0^{(+)}$		
Pr	1	5	10
$\partial_t E_k$	0.020 581	0.115 874	0.151 824
P_S	−0.103 330	−0.097 185	−0.097 212
$-N$	−0.950 970	−1.133 257	−1.200 462
I	−0.095 425	−0.093 619	−0.091 977
M_{hR}	−0.102 894	−0.068 470	−0.060 731
M_{hT}	1.252 300	1.487 674	1.581 481
M_v	0.020 900	0.020 730	0.020 725

IV. PERTURBATION FLOW FIELD

Why the thermocapillary effect can suppress the capillary breakup? In order to provide a clearer explanation for this question, the perturbed flow and temperature distributions for various unstable modes are presented in this section. In Figs. 2–10, the y axis represents

TABLE XVII. The terms of the perturbation energy growth for the non-isothermal jet for the most unstable surface-wave modes $W_0^{(-)}$ at $R_B = 300$, $Bi = 1$, and $S = 10^4$.

Mode	$W_0^{(-)}$		
Pr	1	5	10
α_M	0.839	0.630	0.507
$\partial_t E_k$	0.049 409	0.062 852	0.053 487
P_S	0.035 065	0.041 050	0.038 012
$-N$	−0.022 659	−0.015 382	−0.010 087
I	0.052 736	0.054 590	0.038 231
M_{hR}	0.018 601	0.020 795	0.022 140
M_{hT}	−0.039 304	−0.041 185	−0.036 842
M_v	0.004 971	0.002 985	0.002 033

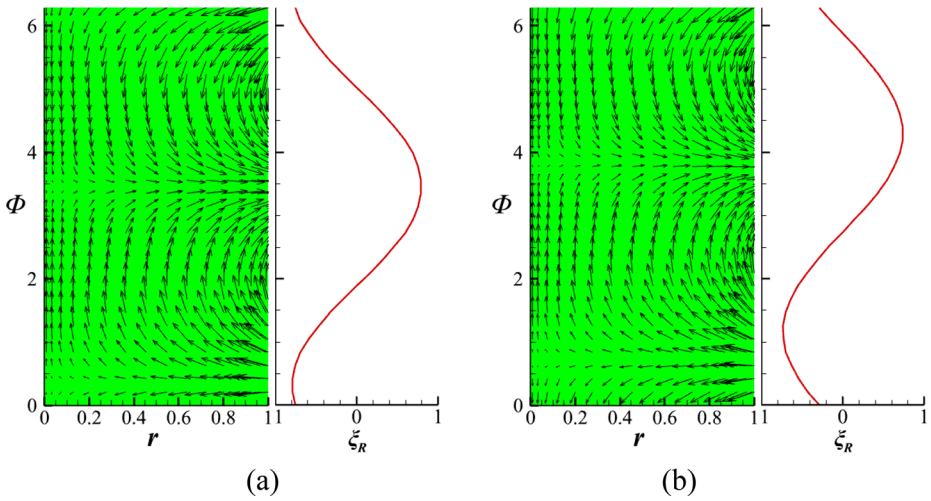

FIG. 2. The perturbation flow field of the most unstable capillary modes $W_0^{(c)}$ at $S = 10^4$: (a) $R_B = 0$ and (b) $R_B = 100$.

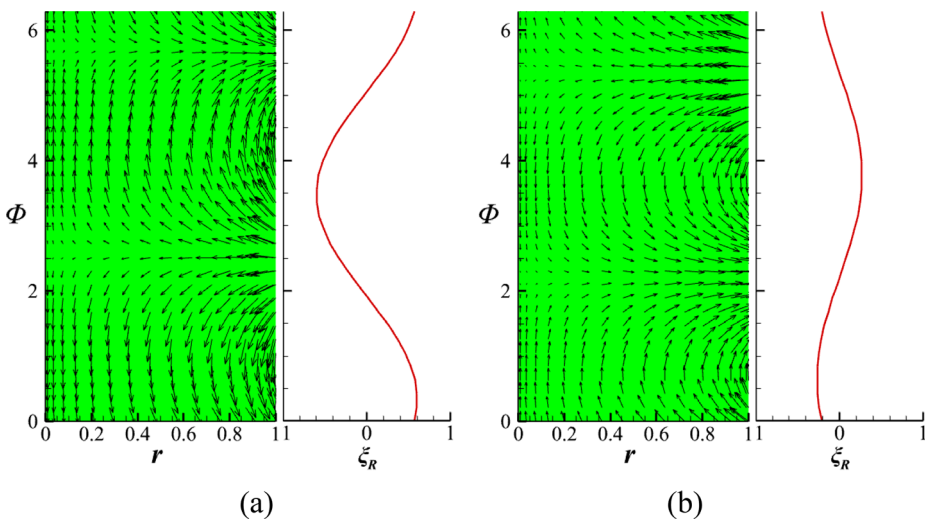

FIG. 3. The perturbation flow field of the most unstable modes at $R_B = 200$ and $S = 10^4$: (a) the capillary mode $W_0^{(c)}$ and (b) the surface-wave $W_0^{(-)}$.

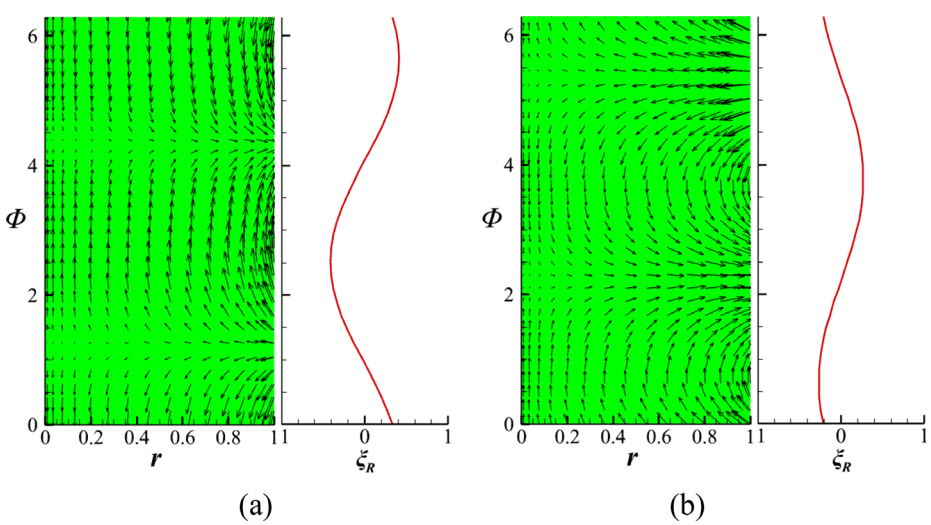

FIG. 4. The perturbation flow field of the most unstable modes at $R_B = 300$ and $S = 10^4$: (a) the capillary mode $W_0^{(c)}$ and (b) the surface-wave mode $W_0^{(-)}$.

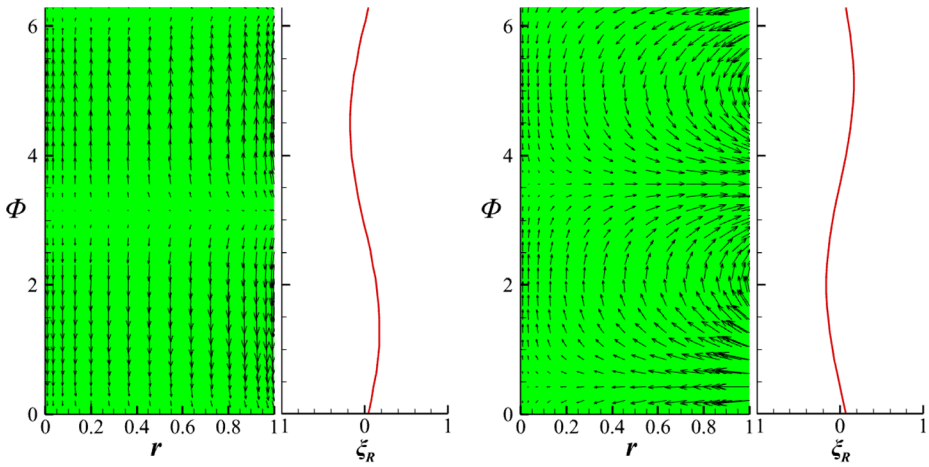

FIG. 5. The perturbation flow field of the most unstable modes at $R_B = 500$ and $S = 10^4$: (a) the capillary mode $W_0^{(c)}$ and (b) the surface-wave mode $W_0^{(-)}$.

the perturbation phase $\Phi = \alpha z + m\theta$. The x axis represents the jet radius, and $\xi_R = \mathrm{Re}\{\hat{\xi}\exp[\mathrm{i}(\alpha z + m\theta)]\}$ represents the surface deformation. For convenience, all complex amplitudes of perturbations $\hat{\phi}$ below are relabeled as ϕ in the following.

A. The "flying jet"

Figures 2–5 show the perturbation flow fields of the most unstable modes at $R_B = 0$–500 and $S = 10^4$. As these modes are isothermal, there are no temperature perturbations. The capillary mode $W_0^{(c)}$ in Fig. 2(a) is stationary, while other capillary modes $W_0^{(c)}$ and the surface-wave modes $W_0^{(-)}$ propagate along the negative y axis. As R_B increases, the amplitude of ξ_R decays for these modes, which effectively prevents the jet from splitting.

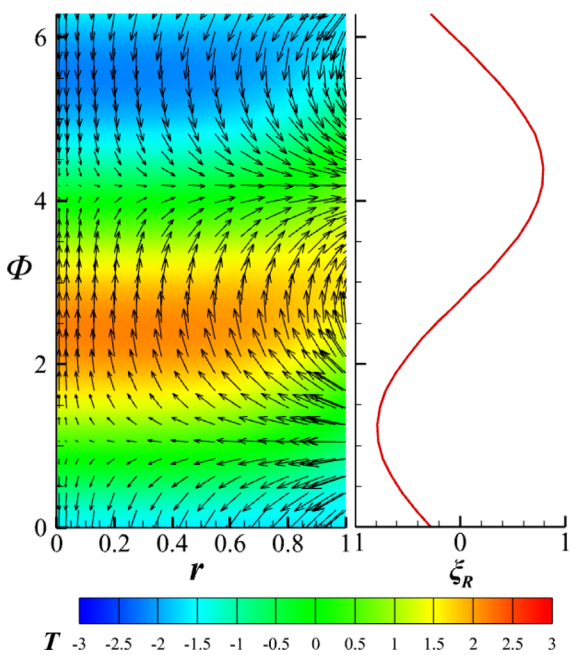

FIG. 6. The perturbation flow field of the most unstable capillary mode $W_0^{(c)}$ at $R_B = 40$, $Pr = 0.5$, $Bi = 1$, and $S = 10^4$.

The reason why the capillary breakup in isothermal jets can be suppressed is explained as follows. Tables III and VII suggest that the main energy source of the capillary instability is the work done by the pressure on the surface (P_S). For the capillary modes $W_0^{(c)}$ ($m = 0$) at $S = 10^4$, the surface pressure perturbation $-p(1) \approx (1 - \alpha_M{}^2)\xi$, where $\alpha_M < 1$(Table VII). In Fig. 2(a), $R_B = 0$, $\bar{w}(1) = \frac{1}{4}S^{-\frac{1}{2}}R_B = 0$, $-p(1) \approx 0.5239\xi$. On the liquid surface $r = 1$, $\Delta\varphi = \arg(u|_{r=1}) - \arg(\xi_R) = 0$, $\int(u|_{r=1}\xi_R)\mathrm{d}r^2 \propto \cos(\Delta\varphi)$ (as shown in Appendix B). So it can be seen from the expression of P_S in Eq. (27) that the capillary mode $W_0^{(c)}$ can extract energy from the surface pressure, which may cause the capillary breakup. However, $\bar{w}(1)$ increases with R_B. According to the continuous boundary condition (21), the phase difference between $u|_{r=1}$ and ξ_R also increases rapidly, leading to the decrease in P_S. Then, the capillary breakup is retarded.

B. Thermocapillary instabilities

Figures 6–10 show the perturbation flow fields of the most unstable modes at $R_B = 40$–500, $Pr = 0.5$, $Bi = 1$, and $S = 10^4$. For the capillary mode $W_0^{(c)}$, there are obvious temperature fluctuations throughout the flow region [Figs. 6, 7(a), 8(a), 9(a), and 10(a)]. For the surface-wave mode $W_0^{(-)}$, the temperature fluctuations are very weak near the interface [Figs. 7(b), 8(b), 9(b), and 10(b)]. On the contrary, the perturbation is concentrated in the thin layer near the liquid surface for the hydrodynamic mode $W_0^{(+)}$ [Figs. 9(c) and 10(c)]. The capillary modes $W_0^{(c)}$ and surface-wave modes $W_0^{(-)}$ propagate along the negative y axis, whereas the hydrodynamic modes $W_0^{(+)}$ propagate in the opposite direction. The surface perturbation amplitude always decreases with the increase in R_B for all modes, which can prevent the capillary breakup.

We provide an explanation for the suppression of capillary breakup in non-isothermal jets as follows. Table IX shows that the work done by surface pressure (P_S) is still the main energy source of the capillary breakup. For the capillary modes $W_0^{(c)}$ ($m = 0$) at $S = 10^4$, $Pr = 0.5$, and $Bi = 1$, the normal stress boundary condition (24) and thermal equilibrium condition (25) on the interface can be simplified as

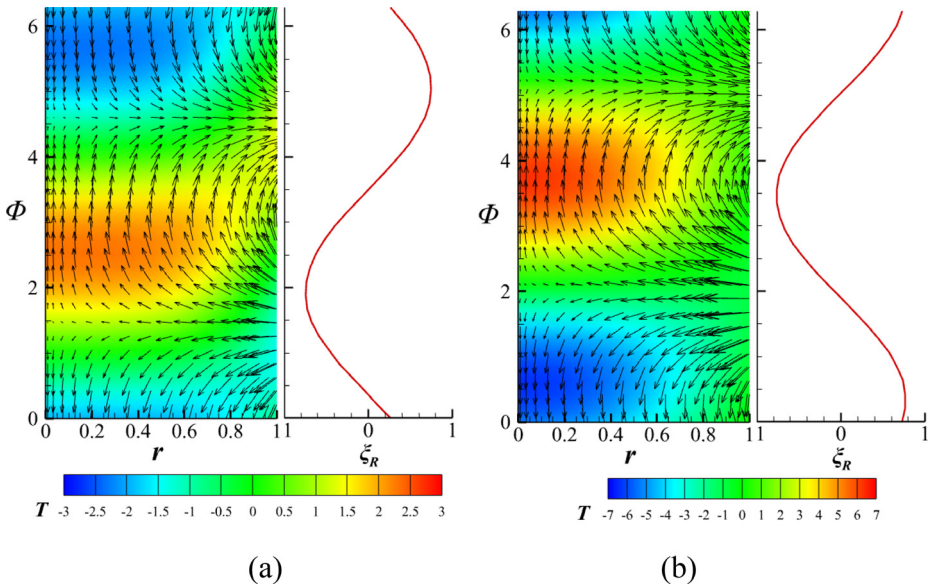

FIG. 7. The perturbation flow field of the most unstable modes at $R_B = 100$, $Pr = 0.5$, $Bi = 1$, and $S = 10^4$: (a) the capillary mode $W_0^{(c)}$ and (b) the surface-wave $W_0^{(-)}$.

$$-p(1) = 2S^{-1}R_B\frac{\partial\xi}{\partial z} - S^{-\frac{1}{2}}\tau_{11} + (1-\alpha^2)\xi + S^{-1}R_B T(1), \tag{30}$$

$$\frac{\partial\xi}{\partial z} = -T(1) - \mathrm{D}T(1) + \frac{1}{8}R_B\xi, \tag{31}$$

respectively. Substituting Eq. (31) in Eq. (30) results in

$$-p(1) = \left(\frac{1}{4}S^{-1}R_B{}^2 + 1 - \alpha^2\right)\xi - S^{-1}R_B[T(1) + 2\mathrm{D}T(1)] - 2S^{-\frac{1}{2}}\mathrm{D}u(1). \tag{32}$$

When R_B is not large, $-p(1) \approx (1-\alpha_M{}^2)\xi$ can still be obtained. In Fig. 7, $R_B = 40$, $\alpha_M = 0.683$, then $\bar{w}(1) = \frac{1}{4}S^{-\frac{1}{2}}R_B = 0.1$, $-p(1) \approx 0.5335\xi$, $\arg(u|_{r=1}) - \arg(\xi_R) \approx 11.6°$. Owing to the proper phase relationship, the key to the capillary breakup is still the work done by surface pressure caused by surface deformation. For $R_B > 200$, $-p(1) \approx (\frac{1}{4}S^{-1}R_B{}^2 + 1 - \alpha_M{}^2)\xi$. However, since $\bar{w}(1)$ is increased by R_B, the phase difference between $u|_{r=1}$ and ξ_R also increases. For example, when $R_B = 500$, $\arg(u|_{r=1}) - \arg(\xi_R) \approx 86.1°$. Therefore, P_S decreases significantly. In addition, in Fig. 10(a), due to the axisymmetric perturbation flow field ($v = 0$), $\arg(w|_{r=1}) - \arg(\xi_R) \approx 171.1°$ and $\arg(w|_{r=1}) - \arg\left(\frac{\partial T}{\partial z}|_{r=1}\right) \approx 167.0°$, we can drive that from Eqs. (28) and (29),

$$M \approx -S^{-1}R_B\int\left(w\xi + w\frac{\partial T}{\partial z}\right)\mathrm{d}^2 r. \tag{33}$$

Then, M becomes the main energy source for the capillary mode. However, the thermocapillary flow also increases the viscous

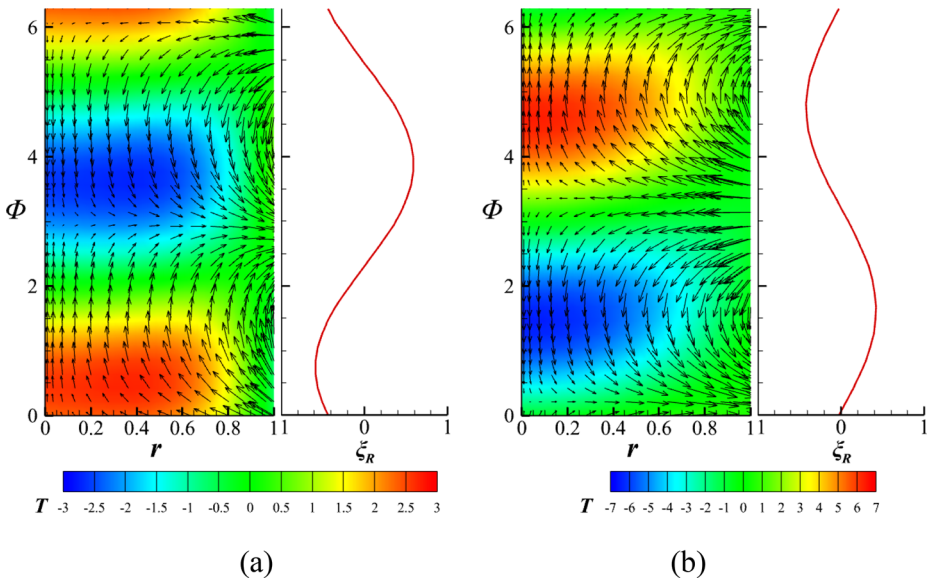

FIG. 8. The perturbation flow field of the most unstable modes at $R_B = 200$, $Pr = 0.5$, $Bi = 1$, and $S = 10^4$: (a) the capillary mode $W_0^{(c)}$ and (b) the surface-wave $W_0^{(-)}$.

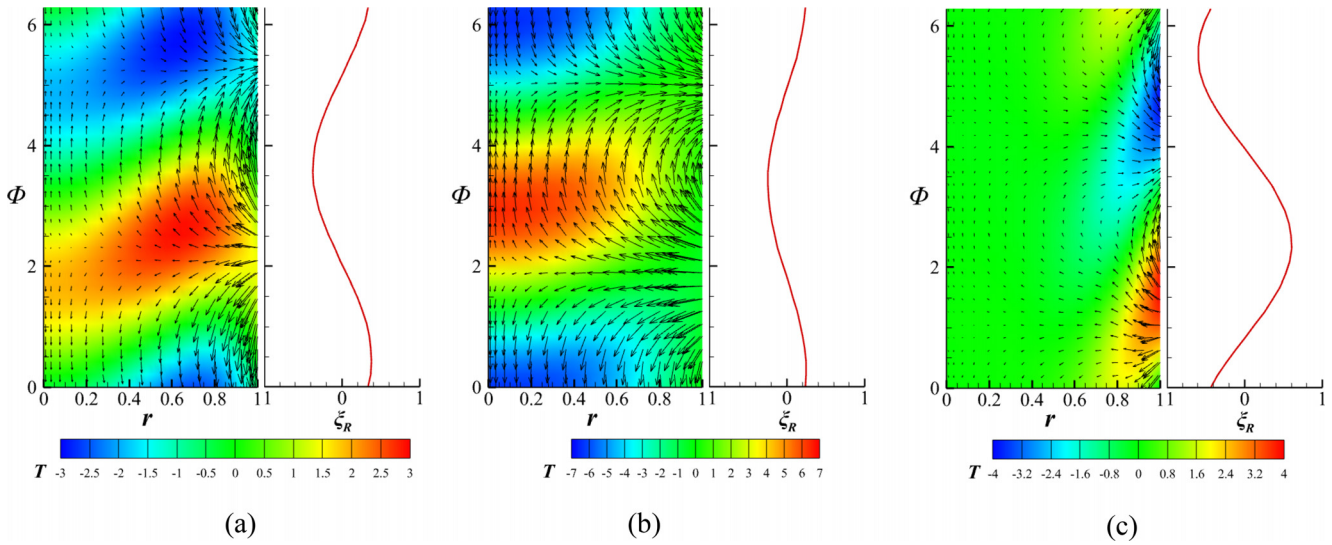

FIG. 9. The perturbation flow field of the most unstable modes at $R_B = 350$, $Pr = 0.5$, $Bi = 1$, and $S = 10^4$: (a) the capillary mode $W_0^{(c)}$; (b) the surface-wave mode $W_0^{(-)}$; and (c) the hydrodynamic mode $W_0^{(+)}$.

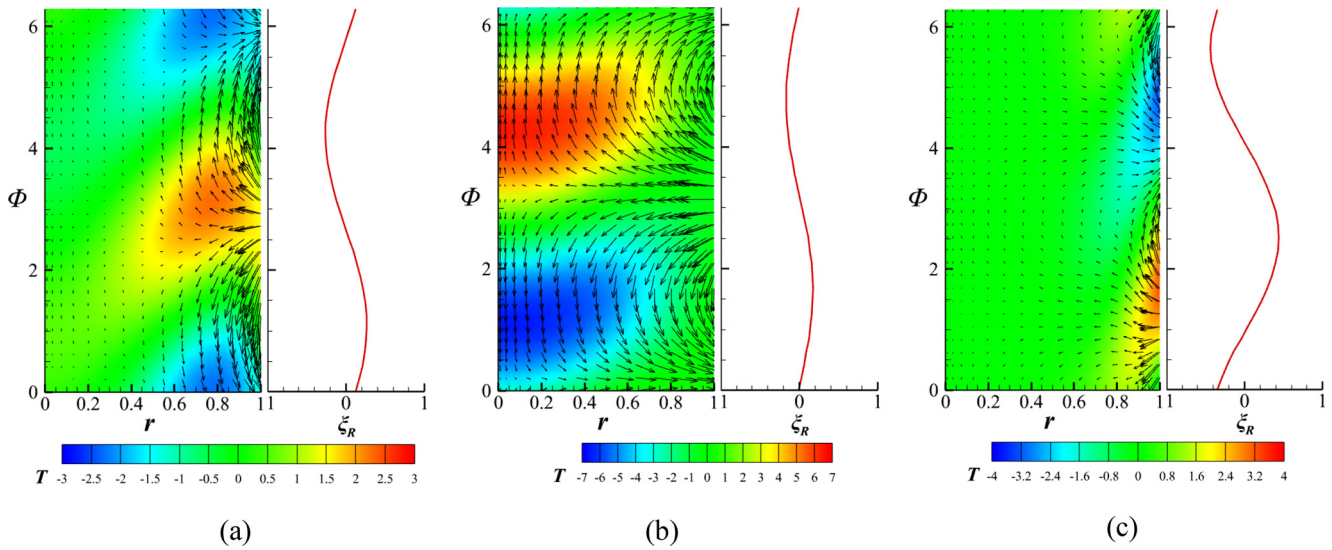

FIG. 10. The perturbation flow field of the most unstable modes at $R_B = 500$, $Pr = 0.5$, $Bi = 1$, and $S = 10^4$: (a) the capillary mode $W_0^{(c)}$; (b) the surface-wave mode $W_0^{(-)}$; and (c) the hydrodynamic mode $W_0^{(+)}$.

dissipation (N) and the energy transferred to the basic flow (I). As a result, the capillary instability is still greatly suppressed.

V. CONCLUSION

In this paper, the energy analysis is performed for instabilities in the cylindrical jet with thermocapillarity. The perturbation flow field is displayed for the capillary mode, surface-wave mode, and hydrodynamic mode. The mechanism of suppressing capillary breakup of the jet is elucidated.

When the Biot number tends to infinity ($Bi \to \infty$), the flow is an isothermal jet driven by the wind stress of the same magnitude as the thermocapillary gradient. The work done by the pressure on the surface (P_S) is the main energy source for the capillary mode. As the Reynolds number of the flying jet (R_B) increases, P_S decreased rapidly. Therefore, the capillary breakup is suppressed.

For a small Prandtl number ($Pr < 1$) and a large Bi ($Bi \geq 1$), when the Reynolds number (R_B) is not too large, P_S remains the main energy source for capillary instability. However, the phase difference between radial velocity and surface deformation increases with R_B, leading to a rapid decrease in P_S. When R_B is large enough, the work done by the stress on the surface (M) is dominant, but the dissipation caused by the viscosity (N) and the energy coming from the basic flow (I) also increase. Therefore, the capillary instability is also suppressed.

The increase in R_B or Pr enhances the energy obtained from the thermocapillary force (M_{hT}), making it the dominant factor and leading to the hydrothermal instability.

For the capillary mode, there are obvious temperature fluctuations throughout the flow region, and for the surface-wave mode, the temperature fluctuations are very weak near the surface, while for the hydrodynamic mode, the hot spot is always found in a thin layer near the liquid surface.

ACKNOWLEDGMENTS

This work has been supported by the National Natural Science Foundation of China (Nos. 11872032 and 12372247), Zhejiang Provincial Natural Science Foundation (No. LY21A020006), and Ningbo Municipality Key Research and Development Program (No. 2022Z213).

AUTHOR DECLARATIONS

Conflict of Interest

The authors have no conflicts to disclose.

Author Contributions

YuWen Sun: Conceptualization (equal); Data curation (lead); Formal analysis (equal); Investigation (equal); Methodology (equal); Software (equal); Validation (equal); Visualization (lead); Writing – original draft (lead); Writing – review & editing (equal). **Kai-xin Hu:** Conceptualization (equal); Funding acquisition (equal); Investigation (equal); Methodology (equal); Project administration (equal); Resources (equal); Supervision (equal); Validation (equal); Writing – original draft (equal); Writing – review & editing (equal). **Qi-Sheng Chen:** Supervision (equal); Validation (equal).

DATA AVAILABILITY

The data that support the findings of this study are available within the article.

APPENDIX A: THE EXPRESSION AFTER ELIMINATING THE PRESSURE TERM

By utilizing Eqs. (17a)–17(c) to eliminate $\hat{p}$, we obtain the following equation:

$$\begin{aligned} &m\{\hat{\tau}_{13} + r\mathrm{D}\hat{\tau}_{13} + \mathrm{i}m\hat{\tau}_{23} + \mathrm{i}\alpha r\hat{\tau}_{33}\} - S^{\frac{1}{2}}\mathrm{i}\alpha m r\bar{w}\hat{w} \\ &\quad - S^{\frac{1}{2}}m r\mathrm{D}\bar{w}\hat{u} - \alpha r\{2\hat{\tau}_{12} + r\mathrm{D}\hat{\tau}_{12} + \mathrm{i}m\hat{\tau}_{22} + \mathrm{i}\alpha r\hat{\tau}_{23}\} \\ &\quad + S^{\frac{1}{2}}\mathrm{i}\alpha^2 r^2\bar{w}\hat{v} = \sigma S^{\frac{1}{2}} r(m\hat{w} - \alpha r\hat{v}), \end{aligned} \tag{A1}$$

$$\begin{aligned} &\alpha\{r\mathrm{D}\hat{\tau}_{13} + r^2\mathrm{D}^2\hat{\tau}_{13} - \hat{\tau}_{13} - \mathrm{i}m\hat{\tau}_{23} + \mathrm{i}m r\mathrm{D}\hat{\tau}_{23} + \mathrm{i}\alpha r^2\mathrm{D}\hat{\tau}_{33}\} \\ &\quad - S^{\frac{1}{2}}\mathrm{i}\alpha^2 r^2(\mathrm{D}\bar{w}\hat{w} + \bar{w}\mathrm{D}\hat{w}) - S^{\frac{1}{2}}\alpha r^2(\mathrm{D}^2\bar{w}\hat{u} + \mathrm{D}\bar{w}\mathrm{D}\hat{u}) \\ &\quad + m r^2\{3\mathrm{D}\hat{\tau}_{12} + r\mathrm{D}^2\hat{\tau}_{12} + \mathrm{i}m\mathrm{D}\hat{\tau}_{22} + \mathrm{i}\alpha\hat{\tau}_{23} + \mathrm{i}\alpha r\mathrm{D}\hat{\tau}_{23}\} \\ &\quad - S^{\frac{1}{2}}\mathrm{i}\alpha m r^2(\bar{w}\hat{v} + r\mathrm{D}\bar{w}\hat{v} + r\bar{w}\mathrm{D}\hat{v}) - S^{\frac{1}{2}}k^2\alpha r^2\bar{w}\hat{u} \\ &\quad - \mathrm{i}k^2 r\{\hat{\tau}_{11} + r\mathrm{D}\hat{\tau}_{11} + \mathrm{i}m\hat{\tau}_{12} + \mathrm{i}\alpha r\hat{\tau}_{13} - \hat{\tau}_{22}\} \\ &= \sigma S^{\frac{1}{2}} r^2(m\hat{v} + m r\mathrm{D}\hat{v} + \alpha\mathrm{D}\hat{w} - \mathrm{i}k^2\hat{u}). \end{aligned} \tag{A2}$$

Using Eqs. (17b) and (17c) to obtain $\hat{p}$ and subsequently substituting it in Eq. (24), we can determine the boundary condition for the normal stress as follows:

$$\begin{aligned} &m r\{2\hat{\tau}_{12} + r\mathrm{D}\hat{\tau}_{12} + \mathrm{i}m\hat{\tau}_{22} + \mathrm{i}\alpha r\hat{\tau}_{23}\} - S^{\frac{1}{2}}\mathrm{i}\alpha m r^2\bar{w}\hat{v} \\ &\quad + \alpha\{\hat{\tau}_{13} + r\mathrm{D}\hat{\tau}_{13} + \mathrm{i}m\hat{\tau}_{23} + \mathrm{i}\alpha r\hat{\tau}_{33}\} - S^{\frac{1}{2}}\alpha r\mathrm{D}\bar{w}\hat{u} \\ &\quad - S^{\frac{1}{2}}\mathrm{i}\alpha^2 r\bar{w}\hat{w} - \mathrm{i}k^2 r(\hat{\tau}_{11} - 2\mathrm{i}\alpha\bar{\tau}_{13}\hat{R}) \\ &\quad + S^{\frac{1}{2}}\mathrm{i}k^2 r(1 - \alpha^2 - m^2)\hat{R} + S^{-\frac{1}{2}}R_B\mathrm{i}k^2 r(\mathrm{D}\bar{T}\hat{R} + \hat{T}) \\ &= \sigma S^{\frac{1}{2}} r(m r\hat{v} + \alpha\hat{w}). \end{aligned} \tag{A3}$$

Here, $k^2 = \alpha^2 + m^2$.

APPENDIX B: THE SURFACE INTEGRAL EXPRESSION FOR THE PRODUCT OF PERTURBATIONS

For the perturbations A and B on the liquid surface,

$$\mathrm{A} = |\mathrm{A}|\sin(\Phi + \varphi_1), \tag{B1}$$

$$\mathrm{B} = |\mathrm{B}|\sin(\Phi + \varphi_2), \tag{B2}$$

the surface integral of their product is

$$\begin{aligned} \int_0^{2\pi}(\mathrm{AB})\mathrm{d}r^2 &= |\mathrm{AB}|\int_0^{2\pi}\sin(\Phi + \varphi_1)\sin(\Phi + \varphi_2)\mathrm{d}\Phi \\ &= \pi|\mathrm{AB}|\cos(\varphi_1 - \varphi_2). \end{aligned} \tag{B3}$$

REFERENCES

[1] J. R. A. Pearson, "On convection cells induced by surface tension," J. Fluid Mech. **4**(5), 489–500 (1958).
[2] E. P. Furlani, B. G. Price, G. Hawkins, and A. G. Lopez, "Thermally induced Marangoni instability of liquid microjets with application to continuous inkjet printing," Proc. NSTI Nanotechnol. **2**, 534–537 (2006), see https://nsti.org/publications/Nanotech/2006/pdf/802.pdf
[3] O. A. Basaran, H. Gao, and P. P. Bhat, "Nonstandard inkjets," Annu. Rev. Fluid Mech. **45**, 85–113 (2013).
[4] G. Loke, W. Yan, T. Khudiyev, G. Noel, and Y. Fink, "Recent progress and perspectives of thermally drawn multimaterial fiber electronics," Adv. Mater. **32**(1), 1904911 (2020).
[5] Y. Zhao, D. Wan, X. Chen, X. Chao, and H. Xu, "Uniform breaking of liquid-jets by modulated laser heating," Phys. Fluids **33**(4), 044115 (2021).
[6] Y. E. Kamis, H. B. Eral, and W. P. Breugem, "Active control of jet breakup and droplet formation using temperature modulation," Phys. Rev. Fluid **6**(10), 103903 (2021).
[7] C. K. W. Tam, "Jet noise: Since 1952," Theor. Comput. Fluid Dyn. **10**(1), 393–405 (1998).
[8] C. Xiao and B. Q. Jia, "Thermal effect on the instability of annular liquid jet," Aerospace **8**(12), 382 (2021).
[9] N. Imaishi, M. K. Ermakov, and W. Y. Shi, "Effects of Pr and pool curvature on thermocapillary flow instabilities in annular pool," Int. J. Heat Mass Transfer **149**, 119103 (2020).
[10] R. Qiao, K. Mu, X. S. Luo, and T. Si, "Instability and energy budget analysis of viscous coaxial jets under a radial thermal field," Phys. Fluids **32**(12), 122103 (2020).
[11] H. M. Li, W. Y. Shi, and M. K. Ermakov, "Thermocapillary flow instabilities of medium Prandtl number liquid in rotating annular pools," Int. J. Heat Mass Transfer **120**, 233–243 (2017).
[12] H. Liu, Z. Zeng, L. M. Yin, Z. H. Qiu, and L. Qiao, "Influence of aspect ratio on the onset of thermocapillary flow instability in annular pool heated from inner wall," Int. J. Heat Mass Transfer **129**, 746–752 (2019).

[13]J. J. Xu and S. H. Davis, "Instability of capillary jets with thermocapillarity," J. Fluid Mech. **161**, 1–25 (1985).
[14]L. Rayleigh, "On the instability of jets," Proc. London Math. Soc. **s1-10**, 4–13 (1878).
[15]M. K. Smith and S. H. Davis, "Instabilities of dynamic thermocapillary liquid layers—Part 2: Surface-wave instabilities," J. Fluid Mech. **132**, 145–162 (1983).
[16]H. A. Dijkstra and P. H. Steen, "Thermocapillary stabilization of the capillary breakup of an annular film of liquid," J. Fluid Mech. **229**, 205–228 (1991).
[17]Y. J. Chen, R. Abbaschian, and P. H. Steen, "Thermocapillary suppression of the Plateau-Rayleigh instability: A model for long encapsulated liquid zones," J. Fluid Mech. **485**, 97–113 (2003).
[18]M. Wanschura, V. M. Shevtsova, H. C. Kuhlmann, and H. J. Rath, "Convective instability mechanisms in thermocapillary liquid bridges," J. Fluid Mech. **7**(5), 912–925 (1995).
[19]M. Levenstam and G. Amberg, "Hydrodynamical instabilities of thermocapillary flow in a half-zone," J. Fluid Mech. **297**, 357–372 (1995).
[20]J. Leypoldt, H. C. Kuhlmann, and H. J. Rath, "Three-dimensional numerical simulation of thermocapillary flows in cylindrical liquid bridges," J. Fluid Mech. **414**, 285–314 (2000).
[21]Y. Wang, Z. Zeng, H. Liu, L. Q. Zhang, L. M. Yin, Y. Xiao, and Y. Liu, "Flow instabilities in thermocapillary liquid bridges between two coaxial disks with different radii," Int. J. Heat Mass Transfer **183**, 122182 (2022).
[22]Y. Wang, L. Q. Zhang, H. Liu, L. M. Yin, Y. Xiao, Y. Liu, and Z. Zeng, "Instabilities of thermocapillary flows in large Prandtl number liquid bridges between two coaxial disks with different radii," Phys. Fluids **34**(6), 062113 (2022).
[23]H. Li, Z. Zeng, L. Q. Zhang, H. Liu, Y. Liu, Y. Wang, Y. Xiao, and L. M. Yin, "Instability mechanisms of thermocapillary liquid bridges between disks of unequal radii," Phys. Fluids **34**(11), 114109 (2022).
[24]I. Chaudhary, P. Garg, G. Subramanian, and V. Shankar, "Linear instability of viscoelastic pipe flow," J. Fluid Mech. **908**, A11 (2021).
[25]Q. S. Chen and W. R. Hu, "Influence of liquid bridge volume on instability of floating half zone convection," Int. J. Heat Mass Transfer **41**(6), 825–837 (1998).
[26]R. Patne, Y. Agnon, and A. Oron, "Thermocapillary instabilities in a liquid layer subjected to an oblique temperature gradient," J Fluid Mech. **906**, A12 (2021).
[27]K. X. Hu, C. Z. Zhao, S. N. Zhang, and Q. S. Chen, "Instabilities of thermocapillary liquid layers with two free surfaces," Int. J. Heat Mass Transfer **173**, 121217 (2021).
[28]K. X. Hu, S. N. Zhang, and Q. S. Chen, "Surface wave instability in the thermocapillary migration of a flat droplet," J. Fluid Mech. **958**, A22 (2023).
[29]M. K. Smith and S. H. Davis, "The instability of sheared liquid layers," J. Fluid Mech. **121**, 187–206 (1982).